

**Crystalline Nickel, Cobalt, and Manganese Antimonates as  
Electrocatalysts for the Chlorine Evolution Reaction**

Journal:	<i>Energy &amp; Environmental Science</i>
Manuscript ID	EE-COM-12-2018-003676.R1
Article Type:	Communication
Date Submitted by the Author:	06-Mar-2019
Complete List of Authors:	Moreno-Hernandez, Ivan; California Institute of Technology, Chemistry and Chemical Engineering Brunschwig, Bruce; California Institute of Technology , Beckman Institute Lewis, Nathan; California Institute of Technology, Chemistry and Chemical Engineering

**Crystalline Nickel, Cobalt, and Manganese Antimonates as Electrocatalysts for the Chlorine Evolution Reaction**

Ivan A. Moreno-Hernandez<sup>1</sup>, Bruce S. Brunschwig<sup>2</sup>, Nathan S. Lewis<sup>1,2,3</sup>

<sup>1</sup>Division of Chemistry and Chemical Engineering, 127-72, California Institute of Technology, Pasadena, CA 91125, USA

<sup>2</sup>Beckman Institute Molecular Materials Research Center, California Institute of Technology, Pasadena, CA 91125, USA

<sup>3</sup>Kavli Nanoscience Institute, California Institute of Technology, Pasadena, CA 91125, USA

\*Correspondence to: [nslewis@caltech.edu](mailto:nslewis@caltech.edu)

**Abstract:**

The chlorine-evolution reaction (CER) is a common, commercially valuable electrochemical reaction, and is practiced at industrial scale globally. A precious metal solid solution of RuO<sub>2</sub> or IrO<sub>2</sub> with TiO<sub>2</sub> is the predominant electrocatalyst for the CER. Herein we report that materials comprised only of non-precious metal elements, specifically crystalline transition-metal antimonates (TMAs) such as NiSb<sub>2</sub>O<sub>x</sub>, CoSb<sub>2</sub>O<sub>x</sub>, and MnSb<sub>2</sub>O<sub>x</sub>, are moderately active, stable catalysts for the electrochemical oxidation of chloride to chlorine under conditions relevant to the commercial chlor-alkali process. Specifically, CoSb<sub>2</sub>O<sub>x</sub> exhibited a galvanostatic potential of 1.804 V vs. NHE at 100 mA cm<sup>-2</sup> of Cl<sub>2</sub>(g) production from aqueous pH = 2, 4.0 M NaCl after 250 h of operation. Studies of the bulk and surface of the electrocatalyst and the composition of the electrolyte before and after electrolysis indicated minimal changes in the surface structure and intrinsic activity of CoSb<sub>2</sub>O<sub>x</sub> as a result of Cl<sub>2</sub>(g) evolution under these conditions.

**Broader context:**

An outstanding challenge in electrochemistry is the development of active, stable catalysts for electrochemical reactions in corrosive environments, such as oxidative reactions in low pH aqueous electrolytes. The conventional solution to this problem involves the use of noble metal oxides, but the scarcity of these materials can limit the global scalability and increase the operating costs of such electrochemical processes. The discovery of stable, active non-precious metal oxide catalysts, such as transition metal antimonates, for electrochemical reactions in such media conditions is thus important for addressing several global challenges such as water electrolysis and decentralized water sanitation.

## Introduction

The chlor-alkali process entails the electrochemical oxidation of chloride to  $\text{Cl}_2(\text{g})$  by the chlorine-evolution reaction (CER) in conjunction with the production of caustic soda (i.e.,  $\text{NaOH}$ ) and  $\text{H}_2$ . The process is performed at industrial scale globally and consumes over 150 TWh of electricity annually. Dimensionally stable anodes, consisting of noble metal oxides of Ir or Ru, are the predominantly used CER anode electrocatalysts.<sup>1-3</sup> The scarcity of Ir and Ru has the potential to constrain industrial use of the chlor-alkali process and limit chlorine use in applications such as water sanitation.<sup>4</sup> Solid solutions of these metal oxides with  $\text{TiO}_2$ ,  $\text{SnO}_2$ ,  $\text{CoO}_x$ , or  $\text{SbO}_x$  have been explored to decrease the amount of Ir and Ru used in CER catalysts.<sup>5-11</sup> The resulting  $\text{RuO}_2$ - $\text{TiO}_2$  anodes exhibit low corrosion rates and are operationally stable for several years. However, Ru is susceptible to the formation of thermodynamically stable species such as soluble Ru chlorides or gaseous Ru oxides, contributing eventually to catalyst degradation.<sup>12, 13</sup> Electrocatalysts for the CER that do not contain noble metals include  $\text{Co}_3\text{O}_4$  and mixed first-row transition metal oxides, but these materials show limited stability under the corrosive conditions required to obtain selectivity for the CER relative to the oxygen-evolution reaction (OER).<sup>1, 10</sup>

Crystalline transition metal antimonates (TMAs) have recently been reported to be active and stable electrocatalysts for water oxidation in acidic electrolytes.<sup>14</sup> Pourbaix diagrams predict that crystalline TMAs such as  $\text{NiSb}_2\text{O}_6$ ,  $\text{CoSb}_2\text{O}_6$ , and  $\text{MnSb}_2\text{O}_6$  should be stable under acidic conditions as well as in the presence of  $\text{Cl}_2(\text{g})$ .<sup>15</sup> Accordingly, we report herein the synthesis of metal oxide films containing crystalline  $\text{MSb}_2\text{O}_6$  ( $\text{M} = \text{Ni}, \text{Co}, \text{Mn}$ ), and report the electrochemical activity and stability of these materials for the CER in acidic  $\text{NaCl}(\text{aq})$ . A primary focus is the electrochemical stability at  $100 \text{ mA cm}^{-2}$  of anodic current density, due to

the relevance of this current density for the commercially practiced chlor-alkali process.<sup>1</sup> The structural, chemical, and dissolution behaviors of crystalline  $\text{MSb}_2\text{O}_6$  for the CER have been evaluated by scanning-electron microscopy, x-ray photoelectron spectroscopy, and inductively coupled plasma mass spectrometry.

## Results

Films of  $\text{NiSb}_2$ ,  $\text{CoSb}_2$ , and  $\text{MnSb}_2$  were prepared by co-sputtering Sb and M (M = Ni, Co, or Mn) onto conductive antimony-doped tin oxide (ATO) substrates.<sup>16</sup> The catalyst loading and stoichiometry of the sputtered metallic films were determined by dissolving the films in 1.0 M  $\text{H}_2\text{SO}_4(\text{aq})$  and measuring the amount of dissolved ions by inductively coupled plasma mass spectrometry (ICP-MS). The loading of transition metal was 375 – 483  $\text{nmol cm}^{-2}$  whereas the Sb loading was 709 – 820  $\text{nmol cm}^{-2}$ , indicating a bulk M:Sb atomic ratio of  $\sim 1:2$  (Table S1). To obtain  $\text{MSb}_2\text{O}_x$  films, the Ni, Co, and Mn metal/Sb films were annealed at 750 °C in air.<sup>14, 17</sup> X-ray diffraction (XRD) data indicated that the  $\text{NiSb}_2\text{O}_x$  and  $\text{CoSb}_2\text{O}_x$  films both contained the tri-rutile  $\text{MSb}_2\text{O}_6$  structure (Figure S1, S2).  $\text{MnSb}_2\text{O}_x$  films contained  $\text{MnSb}_2\text{O}_6$ , orthorhombic  $\text{Sb}_2\text{O}_4$ , and monoclinic  $\text{Sb}_2\text{O}_4$  (Figure S3).  $\text{RuTiO}_x$  films deposited on ATO and annealed at 500 °C exhibited diffraction peaks consistent with a solid solution of rutile-type  $\text{RuO}_2$  and  $\text{TiO}_2$  (Figure S4). Scanning-electron microscopy (SEM) images of the catalyst films indicated that the morphology was different for each film (Figure S5-S8).

The electrochemical behavior of the TMAs was evaluated by cyclic voltammetry (CV), impedance spectroscopy, and chronopotentiometry in 4.0 M  $\text{NaCl}(\text{aq})$  that was adjusted to pH = 2 with 1.0 M  $\text{HCl}(\text{aq})$ . The equilibrium potential for  $\text{Cl}^-/\text{Cl}_2(\text{g})$  was determined to be 1.331 V vs. the normal hydrogen electrode (NHE) under these experimental conditions. For comparison to the behavior of the TMA's, dimensionally stable  $\text{RuTiO}_x$  anodes were also evaluated (details in

Supporting Information). Figure 1a shows typical cyclic voltammograms for NiSb<sub>2</sub>O<sub>x</sub>, CoSb<sub>2</sub>O<sub>x</sub>, MnSb<sub>2</sub>O<sub>x</sub>, and RuTiO<sub>x</sub> at a scan rate of 10 mV s<sup>-1</sup> in the potential range of 1.0 to 2.1 V vs. NHE. Impedance measurements yielded electrode resistances in the range of 20 – 200 Ω for NiSb<sub>2</sub>O<sub>x</sub>, CoSb<sub>2</sub>O<sub>x</sub>, MnSb<sub>2</sub>O<sub>x</sub>, and RuTiO<sub>x</sub> films, hence compensation of 85% of the electrode resistance for electrodes with a geometric area of 0.01 – 0.1 cm<sup>2</sup> resulted in < 30 mV of voltage compensation at  $j_{\text{geo}} = 10 \text{ mA cm}^{-2}$  for most of the catalysts studied herein.

Measurements of the electrochemically active surface area (ECSA) by impedance spectroscopy of the TMAs indicated that NiSb<sub>2</sub>O<sub>x</sub>, CoSb<sub>2</sub>O<sub>x</sub>, MnSb<sub>2</sub>O<sub>x</sub>, and RuTiO<sub>x</sub> films initially had roughness factors of  $1.1 \pm 0.1$ ,  $6.6 \pm 2.5$ ,  $9.0 \pm 5.2$ , and  $8.8 \pm 3.9$ , respectively (Table S2). The initial intrinsic activity of the electrocatalyst films was evaluated by determining the potential required to obtain 1 mA per cm<sup>2</sup> of ECSA from the backward scan, as shown on Figure 1b. The potential at 1 mA cm<sup>-2</sup> of ECSA, which corresponds to a geometric current density of 1 – 15 mA cm<sup>-2</sup> for roughness factors of 1 – 15 as observed herein, is referred to as the intrinsic potential ( $E_i$ ). The NiSb<sub>2</sub>O<sub>x</sub>, CoSb<sub>2</sub>O<sub>x</sub>, MnSb<sub>2</sub>O<sub>x</sub>, and RuTiO<sub>x</sub> films exhibited a 1 mA cm<sup>-2</sup> initial intrinsic potential of  $1.602 \pm 0.018$ ,  $1.652 \pm 0.006$ ,  $1.699 \pm 0.036$ , and  $1.460 \pm 0.010$  V vs. NHE, respectively (Figure 1b, Table S3). The initial  $E_i$  measurements thus indicated that RuTiO<sub>x</sub> was the most active electrocatalyst at this current density, followed by NiSb<sub>2</sub>O<sub>x</sub>, CoSb<sub>2</sub>O<sub>x</sub>, and MnSb<sub>2</sub>O<sub>x</sub>.

Figure 2a shows the electrochemical stability of the TMAs under galvanostatic control at  $j_{\text{geo}} = 100 \text{ mA cm}^{-2}$ . Cyclic voltammetry data were obtained before at 1 h intervals after the chronopotentiometry data were collected (Figure 2b). The potential increased slowly during the 1 h of chronopotentiometry with an abrupt decrease after cyclic voltammograms and impedance data were collected. High frequency transient increases in potential were also observed due to

partial blockage of the catalyst film as a result of  $\text{Cl}_2(\text{g})$  evolution. Figure 3a shows a comparison between the potential obtained from cyclic voltammetry and chronopotentiometry at  $100 \text{ mA cm}^{-2}$  after 85 h of operation for  $\text{CoSb}_2\text{O}_x$  and  $\text{RuTiO}_x$ . In general, the potential observed during extended chronopotentiometry was 10 – 50 mV larger than the potential determined by cyclic voltammetry.

### *NiSb<sub>2</sub>O<sub>x</sub>*

For  $\text{NiSb}_2\text{O}_x$ , the potential at  $j_{\text{geo}} = 100 \text{ mA cm}^{-2}$  under galvanostatic control averaged  $1.874 \pm 0.015 \text{ V vs. NHE}$  during the first 30 min of operation, after which the galvanostatic potential decreased to a minimum value of  $1.842 \pm 0.002 \text{ V vs. NHE}$  for 1 - 2 h of operation (Figure 2a). Then the galvanostatic potential gradually increased and stabilized after 40 h, with an average value of  $2.184 \pm 0.022 \text{ V}$  from 50 – 65 h of operation at  $j_{\text{geo}} = 100 \text{ mA cm}^{-2}$  (Figure 2a). The fluctuation in potential observed for  $\text{NiSb}_2\text{O}_x$  after 30 h was due to a periodic decrease in the potential every 5-10 min associated with bubble detachment. Impedance measurements collected after 1 h intervals of galvanostatic control indicated substantial changes in the capacitance and series resistance of the  $\text{NiSb}_2\text{O}_x$ -coated electrode. The series resistance of the  $\text{NiSb}_2\text{O}_x$  catalyst increased from  $101 \Omega$  to  $165 \Omega$  over 50 h of chronopotentiometry at  $j_{\text{geo}} = 100 \text{ mA cm}^{-2}$ . The increase in series resistance accounted for  $\sim 88 \text{ mV}$  of the observed increase in potential for this film. Impedance data collected at 1 h intervals indicated that  $\text{NiSb}_2\text{O}_x$  exhibited an increase in ECSA from  $\sim 1$  to  $\sim 11$  after 50 h of chronopotentiometry (Figure S9a).

The appearance of Ni and Sb in the electrolyte was measured using ICP-MS (Figure S10a). After 50 h of operation,  $380 \text{ nmol cm}^{-2}$  of Ni and  $45 \text{ nmol cm}^{-2}$  of Sb were present in the electrolyte. The detected concentration corresponded to  $79 \pm 6\%$  of the Ni and  $6 \pm 1\%$  of the Sb

in the original catalyst film, indicating substantial loss of the catalyst layer. XRD of the electrode after electrochemical operation for 50 h indicated that crystalline  $\text{NiSb}_2\text{O}_6$  remained in the catalyst film, and that the mean crystalline size was  $39 \pm 9$  nm before operation and  $11 \pm 1$  nm after operation (Figure S1). The XRD and ICP-MS data of  $\text{NiSb}_2\text{O}_x$  indicate that dissolution leads to a decrease in the mean crystalline size. SEM images indicated a loss of catalyst loading from the surface, while also indicating that the substrate remained coated with a conformal layer of catalyst (Figure S5).

### *CoSb<sub>2</sub>O<sub>x</sub>*

At  $j_{\text{geo}} = 100 \text{ mA cm}^{-2}$ , the galvanostatic potential of  $\text{CoSb}_2\text{O}_x$  initially increased from  $\sim 1.851$  to  $\sim 1.891$  V vs. NHE during the first 1 h of operation, and subsequently remained at  $\sim 1.876$  V vs. NHE after 90 h (Figure 2a). Figure 3a shows the comparison between the potential obtained from cyclic voltammetry and chronopotentiometry between 85 – 90 h of operation. The potential from cyclic voltammetry was  $\sim 1.864$  V vs. NHE, which was  $\sim 12$  mV lower than the galvanostatic potential of  $\sim 1.876$  V vs. NHE measured immediately preceding the cyclic voltammetry scans. Impedance measurements collected after the 1 h galvanostatic intervals indicated minor changes in the ECSA (Figure S9b). The series resistance of  $\text{CoSb}_2\text{O}_x$  remained in the range of 30 - 34  $\Omega$  during the chronopotentiometric experiment, accounting for  $< 10$  mV in the observed variation of the potential. The roughness factor increased from  $\sim 4$  to  $\sim 8$  after 50 h of operation. Less than  $2 \text{ nmol cm}^{-2}$  of Co and  $3 \text{ nmol cm}^{-2}$  of Sb dissolved into the electrolyte after 50 h of operation (Figure S10b), corresponding to a loss of  $\sim 0.6$  nm and  $\sim 0.3$  nm of catalyst or  $0.5 \pm 0.1\%$  Co and  $0.3 \pm 0.1\%$  Sb, respectively. After electrochemical operation for 50 h, XRD data indicated that crystalline  $\text{CoSb}_2\text{O}_6$  remained on the  $\text{CoSb}_2\text{O}_x$  catalyst film, and that the mean crystalline size was  $29 \pm 5$  nm before operation and  $41 \pm 13$  nm after operation

(Figure S2). SEM images indicated that the morphology of  $\text{CoSb}_2\text{O}_x$  films tested for 50 h at  $j_{\text{geo}} = 100 \text{ mA cm}^{-2}$  was similar to the morphology of as-synthesized films (Figure S6). Figure 2c shows the galvanostatic potential for  $\text{CoSb}_2\text{O}_x$  at  $j_{\text{geo}} = 100 \text{ mA cm}^{-2}$  for 250 h. Cyclic voltammetry data was collected at 1 h intervals for the first 45 h, then at 20 h intervals to observe the effect of long-term chronopotentiometry. The activity of  $\text{CoSb}_2\text{O}_x$  was not substantially affected by the duration between cyclic voltammetry scans. The galvanostatic potential for  $\text{CoSb}_2\text{O}_x$  at  $j_{\text{geo}} = 100 \text{ mA cm}^{-2}$  was 1.804 V vs. NHE after 250 h of operation.

### *MnSb<sub>2</sub>O<sub>x</sub>*

Over the first 0.3 h of operation at  $j_{\text{geo}} = 100 \text{ mA cm}^{-2}$ , the galvanostatic potential of  $\text{MnSb}_2\text{O}_x$  initially increased to  $\sim 2.191 \text{ V vs. NHE}$ , followed by a gradual decrease to  $\sim 1.936 \text{ V vs. NHE}$  over 20 h, followed by an average potential of  $1.926 \pm 0.006 \text{ V vs. NHE}$  from 20 to 90 h of operation (Figure 2a). The series resistance of the  $\text{MnSb}_2\text{O}_x$  was between 144 – 168  $\Omega$  during the stability test, accounting for  $\sim 40 \text{ mV}$  in the observed variability in potential. The roughness factor of the  $\text{MnSb}_2\text{O}_x$  film gradually increased from  $\sim 3$  to  $\sim 25$  over 50 h of chronopotentiometry (Figure S9c). ICP-MS of the electrolyte indicated that  $192 \text{ nmol cm}^{-2}$  and  $185 \text{ nmol cm}^{-2}$  of Mn and Sb dissolved in the electrolyte, corresponding to  $46 \pm 3\%$  of Mn and  $26 \pm 1\%$  of Sb in the catalyst film (Figure S10c). After electrochemical operation, XRD confirmed that crystalline  $\text{MnSb}_2\text{O}_6$ , monoclinic  $\text{Sb}_2\text{O}_4$ , and orthorhombic  $\text{Sb}_2\text{O}_4$  remained in the catalyst film, and that the mean crystalline size of  $\text{MnSb}_2\text{O}_x$  was  $3.4 \pm 0.1 \text{ nm}$  before operation and  $3.7 \pm 0.1 \text{ nm}$  after operation (Figure S3). After electrochemical operation, SEM images showed a loss of catalyst loading as well as an increase in film porosity (Figure S7).

### *RuTiO<sub>x</sub>*

Figure 2a shows chronopotentiometry data for RuTiO<sub>x</sub> at  $j_{\text{geo}} = 100 \text{ mA cm}^{-2}$ . The initial galvanostatic potential was  $\sim 1.661 \text{ V vs. NHE}$  and then increased to  $\sim 1.871 \text{ V vs. NHE}$  after 90 h of operation. Figure 3a shows the comparison between the potential obtained from cyclic voltammetry and chronopotentiometry between 85 – 90 h of operation. The potential from cyclic voltammetry was  $\sim 1.828 \text{ V vs. NHE}$ , whereas the potential was  $\sim 1.871 \text{ V vs. NHE}$  from chronopotentiometry immediately preceding the cyclic voltammetry scans. The roughness factor of RuTiO<sub>x</sub> remained essentially constant throughout the chronopotentiometry experiment (Figure S9d). The series resistance of RuTiO<sub>x</sub> electrodes was 17 - 18  $\Omega$  and remained within this range for the duration of the stability test. XRD indicated that RuO<sub>2</sub> and TiO<sub>2</sub> remained in the catalyst film after electrochemical testing, and that the crystalline size was  $17 \pm 1 \text{ nm}$  before operation and  $25 \pm 1 \text{ nm}$  after operation (Figure S4). SEM images indicated an increase in the porosity of the RuTiO<sub>x</sub> films after electrochemical operation (Figure S8). Figure 2c shows the galvanostatic potential for RuTiO<sub>x</sub> at  $j_{\text{geo}} = 100 \text{ mA cm}^{-2}$  for 250 h. Cyclic voltammetry data was collected at 1 h intervals for the first 42 h, then at 20 h intervals to observe the effect of long-term chronopotentiometry. The galvanostatic potential substantially increased during the 20 h chronopotentiometry intervals. The galvanostatic potential at  $j_{\text{geo}} = 100 \text{ mA cm}^{-2}$  for RuTiO<sub>x</sub> was 2.051 V vs. NHE after 250 h of operation.

#### *TMA-free electrodes*

To serve as controls, SbO<sub>x</sub> on ATO and ATO electrodes were prepared without TMA electrocatalyst coatings. These electrodes exhibited a galvanostatic potential  $> 2.331 \text{ V vs. NHE}$  at  $j_{\text{geo}} = 100 \text{ mA cm}^{-2}$  under galvanostatic control. The electrochemical stability of the transition metal oxides NiO<sub>x</sub>, CoO<sub>x</sub>, and MnO<sub>x</sub> was determined using electrocatalyst films that were prepared by the same procedure and transition-metal loading as the MSb<sub>2</sub>O<sub>x</sub> films, except that Sb

was not co-sputtered during the metal deposition. Electrodes consisting of NiO<sub>x</sub> or MnO<sub>x</sub> were unstable for chlorine evolution at  $j_{\text{geo}} = 100 \text{ mA cm}^{-2}$  under galvanostatic control (Figure S11b). CoO<sub>x</sub> electrodes exhibited a potential of  $\sim 1.801 \text{ V vs. NHE}$  at  $j_{\text{geo}} = 100 \text{ mA cm}^{-2}$  under galvanostatic control during the first 6 h of operation, but then the potential increased to  $> 2.051 \text{ V vs. NHE}$  after 8 h of operation (Figure S11b).

### *Intrinsic activity of the electrocatalysts*

The intrinsic activity of the electrocatalyst films was obtained by calculating the intrinsic potential after 1 h intervals of galvanostatic control. After each 1 h interval of chronopotentiometry at  $j_{\text{geo}} = 100 \text{ mA cm}^{-2}$ , cyclic voltammetry and impedance measurements were collected to determine the ECSA,  $E_{\text{cv}}$ , series resistance, and  $E_i$  of the catalyst films. Each intrinsic potential was corrected at 85% of the series resistance determined for each time interval. Figure 3b shows the values of  $E_i$  at  $1 \text{ mA cm}^{-2}$  of ECSA for NiSb<sub>2</sub>O<sub>x</sub>, CoSb<sub>2</sub>O<sub>x</sub>, MnSb<sub>2</sub>O<sub>x</sub>, and RuTiO<sub>x</sub> obtained from these measurements. In general, the qualitative changes in both the potential (Figure 2) and the intrinsic potential (Figure 3b) were similar during operation for most of the electrocatalyst films. Figure 3b shows the intrinsic potential for representative electrodes, whereas Table S3 shows the average and standard deviation for the electrocatalysts studied herein. Figure 3b shows that NiSb<sub>2</sub>O<sub>x</sub> exhibited an  $E_i$  of  $1.624 \text{ V vs. NHE}$  initially, that decreased to a minimum value of  $1.600 \text{ V vs. NHE}$  after 1 h of operation and subsequently increased gradually, to  $1.911 \text{ V vs. NHE}$  after 50 h of operation. CoSb<sub>2</sub>O<sub>x</sub> initially exhibited an  $E_i$  of  $1.656 \text{ V vs. NHE}$ , that gradually increased to  $1.704 \text{ V vs. NHE}$  over 20 h, followed by a stable  $E_i$  of  $1.704\text{-}1.707 \text{ V vs. NHE}$  from 20 to 50 h of operation. MnSb<sub>2</sub>O<sub>x</sub> initially exhibited  $E_i = 1.655 \text{ V vs. NHE}$ , that then increased to  $1.741 \text{ V vs. NHE}$  after 1 h of operation, followed by a gradual increase to  $E_i = 1.789 \text{ V vs. NHE}$  after 50 h of operation. RuTiO<sub>x</sub> exhibited an initial  $E_i$

of 1.443 V vs. NHE, followed by a gradual increase to 1.561 V vs. NHE after 50 h of operation. Table S3 summarizes the changes in intrinsic potential vs. time for  $\text{MSb}_2\text{O}_x$  and  $\text{RuTiO}_x$ .

### *Faradaic Efficiency for $\text{Cl}_2$ Production*

The faradaic efficiency towards the CER was determined using iodometric titration of  $\text{Cl}_2(\text{aq})$  generated at a galvanostatic current density of  $100 \text{ mA cm}^{-2}$ . The iodometric measurements indicated that  $\text{CoSb}_2\text{O}_x$  had the highest faradaic efficiency for the CER ( $97.4 \pm 3.0\%$ ), with  $\text{NiSb}_2\text{O}_x$  ( $96.0 \pm 3.7\%$ ),  $\text{RuTiO}_x$  ( $94.8 \pm 0.9\%$ ), and  $\text{MnSb}_2\text{O}_x$  ( $89.9 \pm 0.8\%$ ) having a slightly lower faradaic efficiency towards the CER but still predominantly evolving  $\text{Cl}_2(\text{g})$  preferentially relative to oxidizing water (Table S2). The production of chlorine was also confirmed with colorimetric measurements using *N,N*-diethyl-*p*-phenylenediamine. Cyclic voltammograms collected in  $\text{pH} = 2.0 \text{ H}_2\text{SO}_4(\text{aq})$ , with current solely attributable to the OER, further confirmed minimal activity towards the OER for  $\text{CoSb}_2\text{O}_x$  in the potential range relevant to the CER (Figure S13).

### *Surface composition as probed by XPS*

Figure 4 shows high-resolution XP spectra of  $\text{NiSb}_2\text{O}_x$ ,  $\text{CoSb}_2\text{O}_x$ , and  $\text{MnSb}_2\text{O}_x$  before and after chronopotentiometry at  $j_{\text{geo}} = 100 \text{ mA cm}^{-2}$ . The Ni 2p spectra of  $\text{NiSb}_2\text{O}_x$  exhibited a peak at  $\sim 856.1 \text{ eV}$ . The peak shapes of  $\text{NiSb}_2\text{O}_x$  were fitted to two Ni(II) components,  $\text{Ni}(\text{OH})_2$  and a peak shape similar to  $\text{Ni}(\text{OH})_2$  but with a 1.0 eV more positive binding energy. The observed binding energy for the more positive contribution is intermediate to that of Ni(II) in  $\text{NiCl}_2$  and  $\text{Ni}(\text{OH})_2$ .<sup>18</sup> In general, the M 2p spectra of TMAs exhibited peak shapes similar to that of the  $\text{M}(\text{OH})_2$  or MO species, but with more positive binding energies.  $\text{NiSb}_2\text{O}_6$  is chemically different than Ni oxides and hydroxides, so the Ni 2p peak binding energy can be different while

remaining in the 2+ oxidation state. Thus, we assign the more positive contribution to Ni(II) in the NiSb<sub>2</sub>O<sub>6</sub> lattice. After electrochemical operation, NiSb<sub>2</sub>O<sub>x</sub> samples exhibited a narrower Ni 2p<sub>3/2</sub> peak at 856.3 ± 0.1 eV compared to NiSb<sub>2</sub>O<sub>x</sub> before electrochemical operation. The peak shape of NiSb<sub>2</sub>O<sub>x</sub> after electrochemical operation could be adequately fit with a peak shape similar to Ni(OH)<sub>2</sub> but shifted positively by 1.0 eV. XP spectra in the Cl, Ir, and Ru regions revealed no detectable Cl, Ir, and Ru before or after electrochemical operation. Mutually similar Sb 3d<sub>3/2</sub> binding energies were observed for NiSb<sub>2</sub>O<sub>x</sub> before (540.4 ± 0.1 eV) and after (540.5 ± 0.1 eV) electrochemical operation. The Sb binding energy is consistent with the samples containing Sb<sup>5+</sup> as well as minor contributions from Sb<sup>3+</sup>.<sup>19</sup> The surface stoichiometry of the NiSb<sub>2</sub>O<sub>x</sub> was 1:1.8 ± 0.1 Ni:Sb prior to electrochemical operation and was 1:3.2 ± 0.1 Ni:Sb after electrochemical operation, indicating that the surface became Sb rich. The catalyst surface coverage was determined by comparing the catalyst metal signal (Ni + Sb) to the overall metal signal of the catalyst and the substrate (Ni+ Sb + Sn), with the signals corrected using the respective relative sensitivity factors. The catalyst coverage was 100% of the surface in both cases.

Before and after electrochemical operation, CoSb<sub>2</sub>O<sub>x</sub> samples exhibited a narrow Co 2p<sub>3/2</sub> XPS peak at 781.2 ± 0.1 eV. The peak shape of Co in CoSb<sub>2</sub>O<sub>x</sub> was similar to that of Co in Co(OH)<sub>2</sub>, but with a ~ 0.5 eV higher binding energy.<sup>20</sup> The observed binding energy is between that of hydrated CoCl<sub>2</sub> and Co(OH)<sub>2</sub>, indicating that Co is in the 2+ oxidation state at the surface of the CoSb<sub>2</sub>O<sub>x</sub> films.<sup>20</sup> The XPS measurements indicate that the oxidation state of Co did not irreversibly change as a result of electrochemical operation. Wide scan XP spectra showed no detectable Cl, Ir, or Ru on the electrodes. The Sb 3d<sub>3/2</sub> binding energy was 540.6 ± 0.1 eV prior to electrochemical operation and 540.3 ± 0.1 eV after electrochemical operation. The XPS

measurements indicate that Sb was present in the 5+ oxidation state prior to electrochemical operation and was in a mixed 5+/3+ oxidation state after electrochemical operation.<sup>19</sup> The surface stoichiometry of  $\text{CoSb}_2\text{O}_x$  was  $1:4.0 \pm 0.1$  Co:Sb prior to electrochemical operation and was  $1:4.5 \pm 0.1$  Co:Sb after electrochemical operation, indicating enrichment of Sb at the surface. The  $\text{CoSb}_2\text{O}_x$  surface catalyst coverage was 100% before and after electrochemical operation.

The  $\text{MnSb}_2\text{O}_x$  samples exhibited a Mn  $2p_{3/2}$  XPS peak at a binding energy of  $641.9 \pm 0.1$  eV before electrochemical operation and  $642.0 \pm 0.1$  eV after electrochemical operation. The binding energies are comparable to Mn in the 2+ oxidation state in  $\text{MnCl}_2$ , and the peak shape was similar to MnO but shifted 0.5 eV more positive.<sup>20, 21</sup> Wide scan XP spectra indicated no detectable Cl, Ir, or Ru on the surface. The Sb  $3d_{3/2}$  peak exhibited a binding energy of  $540.2 \pm 0.1$  eV prior to electrochemical operation and  $540.3 \pm 0.1$  eV after electrochemical operation. The Sb 3d spectra indicated that Sb was present in both the 5+ and 3+ oxidation states before and after electrochemical operation. The surface stoichiometry of  $\text{MnSb}_2\text{O}_x$  was  $1:2.0 \pm 0.1$  Mn:Sb prior to electrochemical operation and  $1:2.7 \pm 0.2$  Mn:Sb after electrochemical operation, indicating surface enrichment of Sb after chlorine evolution. The surface coverage of  $\text{MnSb}_2\text{O}_x$  was  $98.8 \pm 0.4\%$  prior to electrochemical operation and  $96.8 \pm 0.1\%$  after electrochemical operation, indicating partial exposure of the electrocatalyst substrate after chlorine evolution. Table S4 summarizes the observed binding energies of the  $\text{MSb}_2\text{O}_x$  samples and also presents a comparison of the binding energies to literature values. Figure S14 summarizes the roughness factor, potential, stoichiometry, and crystalline size of the catalysts studied herein after different durations of galvanostatic operation.

## Discussion

### *Trends in Catalyst Intrinsic Activity*

The initial intrinsic activity measurements of TMAs under chlorine evolution indicate an activity trend of  $\text{NiSb}_2\text{O}_x > \text{CoSb}_2\text{O}_x > \text{MnSb}_2\text{O}_x$ . Previous studies of the intrinsic OER activity of  $\text{MSb}_2\text{O}_x$  in acidic electrolytes indicated an OER activity trend of  $\text{NiSb}_2\text{O}_x \approx \text{MnSb}_2\text{O}_x$ , while  $\text{CoSb}_2\text{O}_x$  was not previously examined for the OER.<sup>14</sup> Further improvements in the activity of TMAs towards chlorine evolution could possibly be achieved via solid solutions, as has been demonstrated for OER electrocatalysts and/or by use of other transition metals in the  $\text{SbO}_x$  framework.<sup>14</sup> Notably,  $\text{CoSb}_2\text{O}_x$  had the highest CER activity after extended operation (Figure 2, Figure S13). While the  $\text{CoSb}_2\text{O}_x$  catalyst had an initial intrinsic potential that was  $\sim 190$  mV higher than  $\text{RuTiO}_x$ , this difference decreased to  $\sim 140$  mV after 50 h of chronopotentiometry, due to the intrinsic potential of  $\text{RuTiO}_x$  increasing ( $\sim 1.3$  mV  $\text{h}^{-1}$ ) while the  $\text{CoSb}_2\text{O}_x$  intrinsic potential remained constant after an initial increase (Figure 3b). The high stability of the electrochemical activity of  $\text{CoSb}_2\text{O}_x$  relative to  $\text{RuTiO}_x$  suggests that  $\text{CoSb}_2\text{O}_x$  electrodes could have active electrocatalytic CER lifetimes exceeding those of  $\text{RuTiO}_x$ .

During chlorine evolution, the surface composition of the TMAs changed, and correlated with changes in the intrinsic activity of the catalyst films. As indicated by XPS,  $\text{NiSb}_2\text{O}_x$  and  $\text{MnSb}_2\text{O}_x$  exhibited surface compositions that were very similar to their bulk composition ( $\sim 1:2$  M:Sb), but  $\text{CoSb}_2\text{O}_x$  exhibited substantial initial surface enrichment of Sb (1:4 Co:Sb) despite having a bulk composition of  $\sim 1:2$  M:Sb (Figure 4, Table S1). The surface enrichment of  $\text{CoSb}_2\text{O}_x$  is consistent with previous reports for cobalt antimony oxides.<sup>22</sup>

The intrinsic potential of  $\text{NiSb}_2\text{O}_x$  films initially decreased by 32 mV during operation, followed by an increase of 300 mV (Figure 3). While the Ni 2p spectra indicate that Ni is in the

2+ oxidation state before and after electrochemical operation, Ni(II) compounds such as NiO, Ni(OH)<sub>2</sub>, NiCl<sub>2</sub>, and NiSb<sub>2</sub>O<sub>6</sub> have different peak binding energies despite having the same formal oxidation state. Fitting of the Ni 2p peak shape can reveal which species are present on the surface.<sup>23</sup> The spectrum of NiSb<sub>2</sub>O<sub>x</sub> could not be adequately fit with the fitting parameters of previously reported species, so NiSb<sub>2</sub>O<sub>x</sub> was fit by using the peak shape of Ni(OH)<sub>2</sub> shifted positively by 1.0 eV. The observed contributions at 1.0 eV more positive binding energies could correspond to Ni(II) in the NiSb<sub>2</sub>O<sub>6</sub> lattice. Fitting the Ni 2p data of NiSb<sub>2</sub>O<sub>x</sub> before electrochemical operation with the proposed NiSb<sub>2</sub>O<sub>6</sub> fit revealed low binding energy contributions that are consistent with Ni hydroxide species (Figure 4a). The surface composition of the NiSb<sub>2</sub>O<sub>x</sub> was similar to its bulk composition (~1:2 M:Sb), but the XPS data suggest that the surface was covered by multiple Ni(II) species, such as NiSb<sub>2</sub>O<sub>6</sub>, NiO<sub>x</sub>, and Ni(OH)<sub>2</sub> (Figure 4a). NiO<sub>x</sub> and Ni(OH)<sub>2</sub> are expected to be readily removed from the surface due to thermodynamically favored dissolution processes under the operating conditions, and NiO<sub>x</sub> is unstable towards the CER (Figure S11b). Loss of NiO<sub>x</sub> and Ni(OH)<sub>2</sub> in the first hour of operation could explain the initial improvement in catalytic activity, if these species had a detrimental effect on the activity. After 50 h of operation, NiSb<sub>2</sub>O<sub>x</sub> exhibited substantial surface enrichment of Sb, as indicated by the ~ 80% increase of Sb relative to Ni (Figure 4a, 4d). The Ni in NiSb<sub>2</sub>O<sub>x</sub> exhibited a 2+ oxidation state before and after electrochemical operation. Contributions from Ni(OH)<sub>2</sub> or NiO<sub>x</sub> decreased after electrochemical operation as indicated by the Ni 2p XPS data, suggesting that the surface Ni either dissolved or is in a NiSb<sub>2</sub>O<sub>6</sub> lattice and did not undergo conversion to stable Ni oxides or (oxy)hydroxides.

The intrinsic potential of MnSb<sub>2</sub>O<sub>x</sub> increased by ~ 85 mV in the first hour of operation but increased by only another 20 mV in the next 50 h. The oxidation states of both Mn and Sb

did not change substantially after electrochemical operation (Figure 4b, 4e). However, the surface of the  $\text{MnSb}_2\text{O}_x$  became Sb rich, as indicated by the  $\sim 39\%$  increase in Sb at the surface compared to Mn as measured by XPS. The increase in Sb at the surface, without a substantial change in binding energy, suggests that Sb remained in the 5+ oxidation state. The substantially smaller change in potential after 50 h for  $\text{MnSb}_2\text{O}_x$  ( $\Delta E_i = 134$  mV) as compared to  $\text{NiSb}_2\text{O}_x$  ( $\Delta E_i = 287$  mV) might be due to a lower surface coverage of  $\text{SbO}_x$  species (Figure 3, 4).

The surface of  $\text{CoSb}_2\text{O}_x$  differed substantially from the surface of  $\text{NiSb}_2\text{O}_x$  or  $\text{MnSb}_2\text{O}_x$ .  $\text{CoSb}_2\text{O}_x$  exhibited substantial initial surface enrichment of Sb (1:4 Co:Sb) prior to electrochemical operation in contrast to both  $\text{NiSb}_2\text{O}_x$  and  $\text{MnSb}_2\text{O}_x$  that had an initial surface M:Sb ratio close to their bulk stoichiometry of  $\sim 1:2$ . The  $\text{CoSb}_2\text{O}_x$  exhibited an increase in surface Sb (1:4.5 Co:Sb) after electrochemical operation ( $\sim 13\%$ ), again in contrast to  $\text{NiSb}_2\text{O}_x$  and  $\text{MnSb}_2\text{O}_x$  whose Sb surface enrichment after electrochemical operation increased  $\sim 80\%$ , and  $\sim 39\%$ , respectively. However, in all cases after electrochemical operation the surfaces were significantly enriched in Sb relative to the transition metal. As opposed to the  $\text{NiSb}_2\text{O}_x$  and  $\text{MnSb}_2\text{O}_x$  electrodes, the  $\text{CoSb}_2\text{O}_x$  electrode exhibited a minimal change in intrinsic potential after 50 h ( $\Delta E_i = 48$  mV), which correlates with the minimal change in Sb enrichment at the surface. The initial oxidation states of Co and Sb at the surface were 2+ and 5+, in accord with expectations for stoichiometric  $\text{CoSb}_2\text{O}_6$  (Figure 4). After electrochemical testing,  $\text{CoSb}_2\text{O}_x$  exhibited a decrease of 0.3 eV in Sb  $3d_{5/2}$  binding energy, whereas  $\text{NiSb}_2\text{O}_x$  and  $\text{MnSb}_2\text{O}_x$  both exhibited an increase in the binding energy of Sb  $3d_{5/2}$  ( $\Delta E = 0.1$  eV). The decrease in binding energy of Sb in  $\text{CoSb}_2\text{O}_x$  could be related to the Sb-rich layer on the surface of  $\text{CoSb}_2\text{O}_x$ , which is not present in the nearly stoichiometric surface of the  $\text{NiSb}_2\text{O}_x$  and  $\text{MnSb}_2\text{O}_x$  films before electrochemical operation. Cyclic voltammetry data were collected at more negative potentials

than thermodynamic potential for chlorine evolution, and cathodic current was observed at such potentials (Figure 2b). Further studies to determine the catalytically active site of TMAs could allow more detailed elucidation of the electrocatalytic role of the Sb oxidation state.

### *Comparison of Activity to Other CER Electrocatalysts*

Previous studies of chlorine evolution catalysts have included  $\text{Co}_3\text{O}_4$ , which exhibits  $\eta \sim 1.951$  V vs. NHE at  $j_{\text{geo}} = 100$   $\text{mA cm}^{-2}$ , with an estimated catalyst roughness factor of  $> 3,000$ .<sup>24</sup> Nanostructured  $\text{RuO}_2\text{-TiO}_2$  electrodes exhibit  $\eta \sim 2.041$  V vs. NHE at  $j_{\text{geo}} = 250$   $\text{mA cm}^{-2}$ , with an estimated roughness factor of  $\sim 390$ .<sup>25</sup>  $\text{Ir}_{0.7}\text{Ta}_{0.3}\text{O}_y$  films exhibit  $\eta > 2.331$  V vs. NHE at  $j_{\text{geo}} = 30$   $\text{mA cm}^{-2}$  in  $\text{pH} = 7$ , 50 mM  $\text{NaCl(aq)}$  electrolyte.<sup>26</sup> Mesoporous  $\text{Ru/TiO}_2$  dimensionally stable anodes exhibit  $\eta \sim 1.981$  V vs. NHE at  $j_{\text{geo}} = 100$   $\text{mA cm}^{-2}$  in 4.0 M  $\text{NaCl(aq)}$ ,  $\text{pH} = 3.0$  electrolyte.<sup>8</sup> The  $\sim 1.871$  V vs. NHE galvanostatic potential at  $j_{\text{geo}} = 100$   $\text{mA cm}^{-2}$  reported herein for  $\text{RuTiO}_x$  between 85 – 90 h of operation is comparable to previous reports of noble metal oxides for chlorine evolution (Figure 2a).  $\text{CoSb}_2\text{O}_x$  exhibits a galvanostatic potential of  $\sim 1.804$  V vs. NHE at  $j_{\text{geo}} = 100$   $\text{mA cm}^{-2}$  after 250 h, which is lower than some previous reports for noble metal oxides and is lower than the potential observed herein for  $\text{RuTiO}_x$  after extended operation (Figure 2c). The catalyst loading and roughness factor used herein were both relatively low, to facilitate determination of the intrinsic properties of the electrocatalysts. Consequently, the potential of the TMAs could be improved further by increasing the catalyst loading and roughness, to expose additional catalytically active sites without changing the geometric area of the electrode. Due to the deactivation of  $\text{RuTiO}_x$  during chronopotentiometry and the comparatively high electrochemical stability of  $\text{CoSb}_2\text{O}_x$ , after 250 h of operation  $\text{CoSb}_2\text{O}_x$  exhibited a galvanostatic potential  $\sim 247$  mV lower than that of  $\text{RuTiO}_x$  ( $\sim 2.051$  V vs. NHE). This behavior suggests that  $\text{CoSb}_2\text{O}_x$  may constitute a promising alternative to  $\text{RuTiO}_x$  for the

chlor-alkali process and other processes that require the CER. Co and Sb are substantially more abundant than Ru, and their annual molar production rates are over 5,000 times higher than Ru.<sup>27</sup> The high abundance of both Co and Sb relative to Ru is reflected in the market price of these elements, which reflects a substantially lower price per mole of metals for  $\text{CoSb}_2\text{O}_x$  ( $\sim 2$  USD  $\text{mol}^{-1}$ ) compared to the price per mol for the commercially used  $\text{Ru}_{0.3}\text{Ti}_{0.7}\text{O}_x$  ( $\sim 153$  USD  $\text{mol}^{-1}$ ) catalyst.<sup>27</sup>

### *Trends in Catalyst Stability*

Under CER conditions, the chemical stability of the TMA's decreased in the order  $\text{CoSb}_2\text{O}_x > \text{MnSb}_2\text{O}_x > \text{NiSb}_2\text{O}_x$ .  $\text{CoSb}_2\text{O}_x$  exhibited the lowest dissolution rate, with  $< 0.6$  nm of Co ( $\sim 2$  nmol  $\text{cm}^{-2}$ ) and  $< 0.3$  nm of Sb lost ( $\sim 3$  nmol  $\text{cm}^{-2}$ ) from the surface after 50 h of operation (Figure S10b). Possible explanations for the appearance of M and Sb in the electrolyte include dissolution of oxide species that did not form the stable  $\text{MSb}_2\text{O}_6$  phase, and/or chemically or electrochemically driven dissolution processes. Additionally, mechanical detachment of  $\text{MSb}_2\text{O}_6$  particles could lead to changes in the catalyst loading that cannot be detected with ICP-MS. The small amount of dissolved Co and Sb ( $\sim 4 \times 10^{-9}$  mol  $\text{cm}^{-2}$ ) for  $\text{CoSb}_2\text{O}_x$ , compared to the charge passed during the stability experiments ( $\sim 1.8 \times 10^4$  C  $\text{cm}^{-2}$ ), suggests a turnover number of  $> 2 \times 10^7$  based on the dissolution observed per charge passed, indicating that faradaic dissolution pathways are unlikely to be dominant. After 250 h at  $j_{\text{geo}} = 100$  mA  $\text{cm}^{-2}$ , the  $\text{CoSb}_2\text{O}_x$  electrocatalyst has thus turned-over  $\sim 10^6$  equivalents of  $\text{Cl}_2$  without substantial degradation. While the dissolution studies indicate that  $\text{CoSb}_2\text{O}_x$  has high electrochemical stability, industrial applications will require toxicology studies to determine possible exposure routes to Co and Sb. Similar studies have been conducted for polyethylene terephthalate bottles used for water consumption containing an antimony trioxide polymerization

catalyst.<sup>28</sup> The high turnover number suggest that Sb could be present at  $\sim 0.05$  ppm concentrations in the products of the chlor-alkali process utilizing a  $\text{CoSb}_2\text{O}_x$  electrocatalysts. However, since chlorine is usually used in the 1 - 3 ppm range to disinfect water, the dilution of chlorine would also lead to the dilution of Sb, which could lead to an Sb concentration of  $\sim 0.15$  parts-per-trillion. Antimony is limited to 5 - 6 ppb in drinkable water in the United States and the European Union, which is  $\sim 3 \times 10^4$  greater than the concentration expected for water treated with diluted chlorine generated with a  $\text{CoSb}_2\text{O}_x$  catalyst under the specific experimental conditions evaluated in this work. The high chemical and electrochemical stability of  $\text{CoSb}_2\text{O}_x$ , as indicated by minimal changes in catalyst morphology, intrinsic potential, and surface oxidation, suggest that  $\text{CoSb}_2\text{O}_x$  and possibly other TMAs could be viable materials for chlorine evolution in devices requiring abundant and stable electrocatalysts under industrially relevant operational conditions.

## Conclusion

$\text{NiSb}_2\text{O}_x$ ,  $\text{CoSb}_2\text{O}_x$ , and  $\text{MnSb}_2\text{O}_x$  were found to be moderately active chlorine evolution catalysts for  $> 60$  h at  $j_{\text{geo}} = 100 \text{ mA cm}^{-2}$  in 4.0 M  $\text{NaCl(aq)}$ ,  $\text{pH} = 2.0$  electrolyte.  $\text{CoSb}_2\text{O}_x$  exhibited the highest stability and selectivity among the TMAs tested herein, with  $< 1$  nm of metals lost after extended electrochemical operation. After 250 h of operation, the galvanostatic potential of  $\text{CoSb}_2\text{O}_x$  at  $j_{\text{geo}} = 100 \text{ mA cm}^{-2}$  was lower than that of dimensionally stable  $\text{RuTiO}_x$ . The results suggest that TMAs could be further modified to potentially yield stable catalysts for chlorine evolution with lifetimes and selectivity comparable to or greater than that of dimensionally stable anodes such as  $\text{RuTiO}_x$ .

## Acknowledgements

This work was supported through the Office of Science of the U.S. Department of Energy (DOE) under award no. DE-SC0004993 to the Joint Center for Artificial Photosynthesis, a DOE Energy Innovation Hub. I.A.M.-H. acknowledges a National Science Foundation Graduate Research Fellowship under Grant No. DGE-1144469. We thank Dr. K. Papadantonakis for assistance with editing the manuscript, and C. Finke for assistance with iodometric measurements.

### Figures:

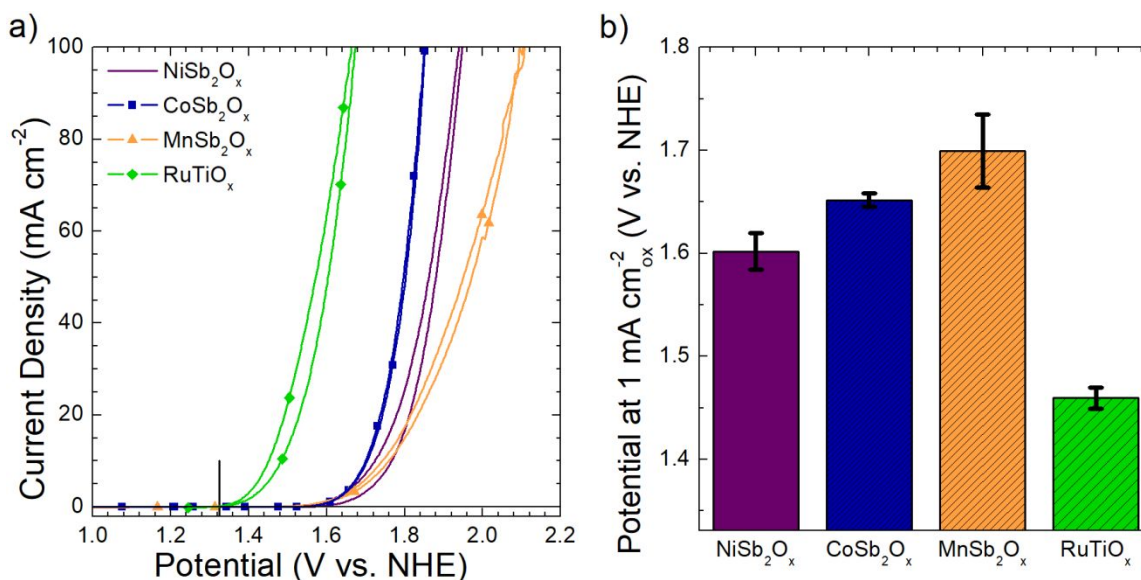


**Figure 1.** Initial electrochemical behavior of NiSb<sub>2</sub>O<sub>x</sub>, CoSb<sub>2</sub>O<sub>x</sub>, MnSb<sub>2</sub>O<sub>x</sub>, and RuTiO<sub>x</sub> in pH = 2.0, 4.0 M NaCl(aq) electrolyte. (a) Cyclic voltammetry of NiSb<sub>2</sub>O<sub>x</sub>, CoSb<sub>2</sub>O<sub>x</sub>, MnSb<sub>2</sub>O<sub>x</sub>, and RuTiO<sub>x</sub> at a scan rate of 10 mV s<sup>-1</sup>. (b) Intrinsic potential of NiSb<sub>2</sub>O<sub>x</sub>, CoSb<sub>2</sub>O<sub>x</sub>, MnSb<sub>2</sub>O<sub>x</sub>, and RuTiO<sub>x</sub> determined from cyclic voltammetry data at 1 mA cm<sup>-2</sup> of electrochemically active surface area. The vertical black line indicates the thermodynamic potential for chlorine evolution in 4.0 M NaCl(aq).

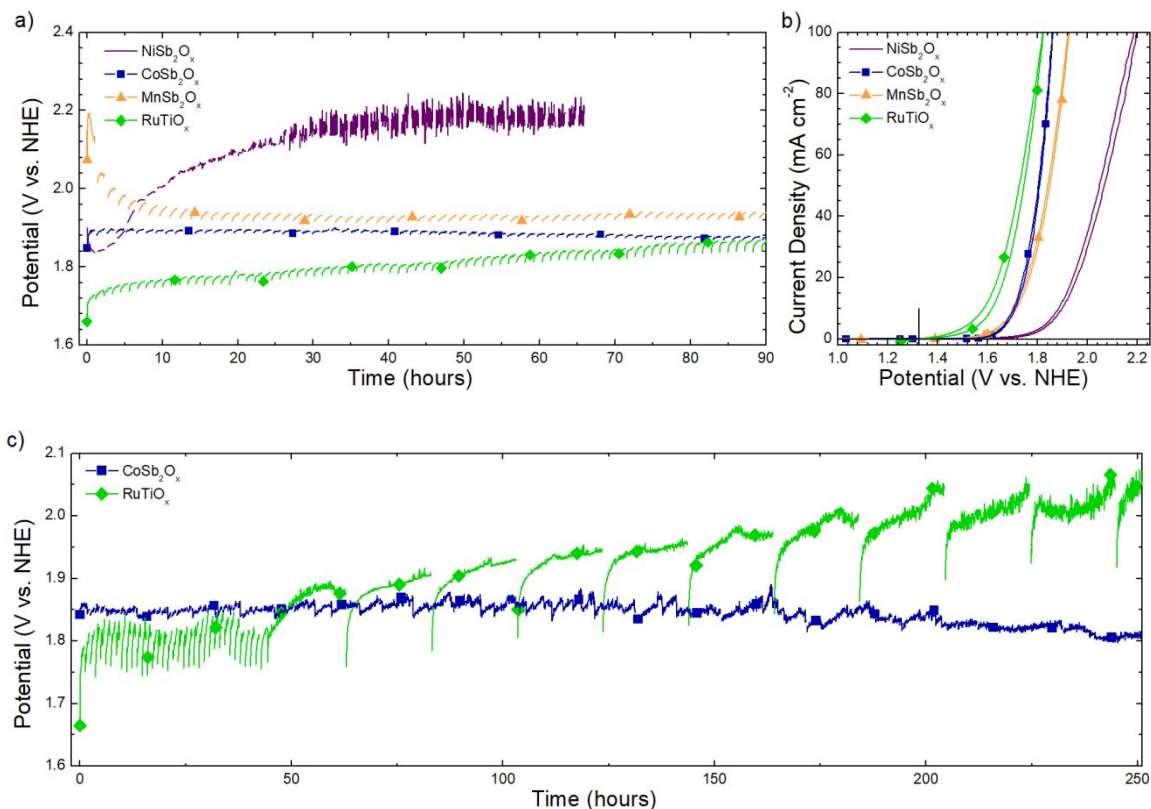


**Figure 2.** a) Chronopotentiometry of  $\text{MSb}_2\text{O}_x$  films and  $\text{RuTiO}_x$ , at  $j_{\text{geo}} = 100 \text{ mA cm}^{-2}$  in 4.0 M NaCl(aq), pH = 2.0 electrolyte. b) Cyclic voltammetry of  $\text{MSb}_2\text{O}_x$  films and of  $\text{RuTiO}_x$ , after the chronopotentiometry stability experiments, at  $j_{\text{geo}} = 100 \text{ mA cm}^{-2}$  in 4.0 M NaCl(aq), pH = 2.0 electrolyte. The cyclic voltammetry data shown were recorded after operation for 65 h for  $\text{NiSb}_2\text{O}_x$  and 90 h for  $\text{MnSb}_2\text{O}_x$ ,  $\text{CoSb}_2\text{O}_x$  and  $\text{RuTiO}_x$ . c) Chronopotentiometry of  $\text{CoSb}_2\text{O}_x$  and  $\text{RuTiO}_x$  at  $j_{\text{geo}} = 100 \text{ mA cm}^{-2}$  in 4.0 M NaCl(aq), pH = 2.0 electrolyte for 250 h. Cyclic voltammetry scans were collected at 1 h intervals for the first ~ 45 h, then collected at 20 h intervals from 45 – 250 h.

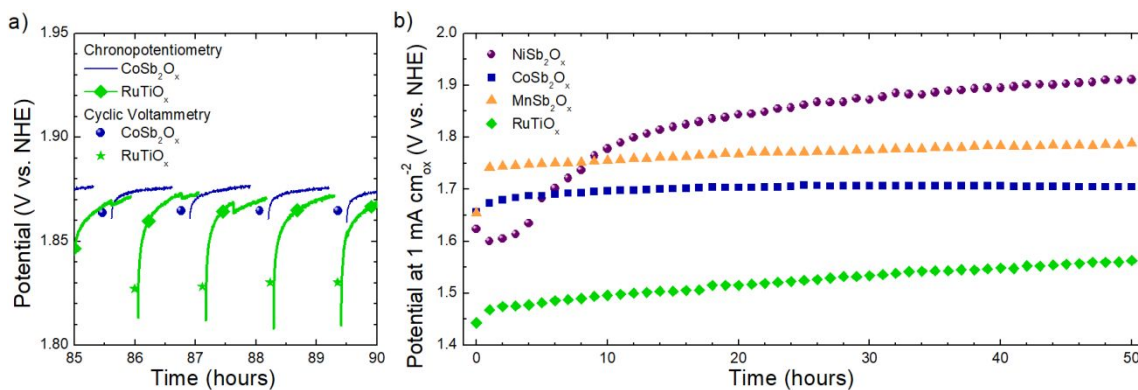


**Figure 3.** a) Comparison between potential after extended operation obtained from cyclic voltammetry and chronopotentiometry at  $j_{\text{geo}} = 100 \text{ mA cm}^{-2}$  for CoSb<sub>2</sub>O<sub>x</sub> and RuTiO<sub>x</sub>. b) Intrinsic potential,  $E_i$ , at  $1 \text{ mA cm}^{-2}$  of electrochemically active surface area determined from cyclic voltammetry and impedance measurements, collected at 1 h intervals in between chronopotentiometry measurements at  $j_{\text{geo}} = 100 \text{ mA cm}^{-2}$ , for NiSb<sub>2</sub>O<sub>x</sub>, CoSb<sub>2</sub>O<sub>x</sub>, MnSb<sub>2</sub>O<sub>x</sub>, and RuTiO<sub>x</sub>.

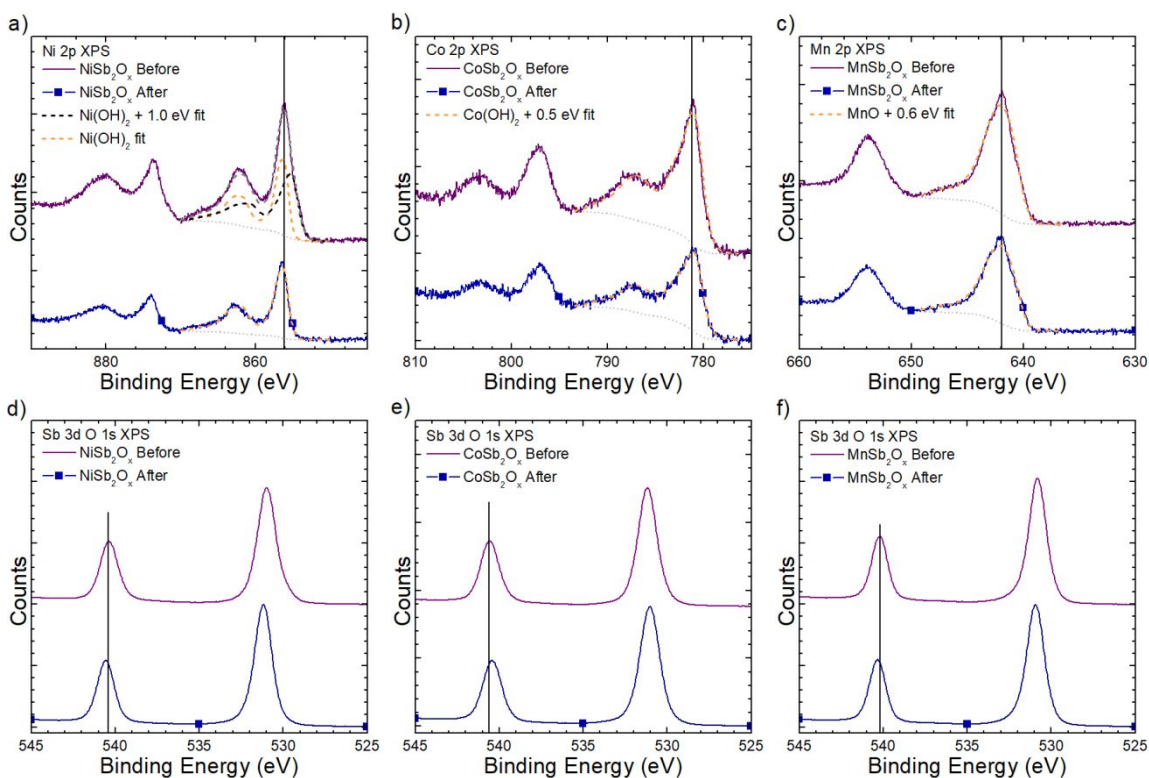


**Figure 4.** X-ray photoelectron spectra of TMAs before and after electrochemical operation: a) NiSb<sub>2</sub>O<sub>x</sub> Ni 2p spectra, b) CoSb<sub>2</sub>O<sub>x</sub> Co 2p spectra, c) MnSb<sub>2</sub>O<sub>x</sub> Mn 2p spectra, and Sb 3d and O 1s spectra of d) NiSb<sub>2</sub>O<sub>x</sub>, e) CoSb<sub>2</sub>O<sub>x</sub>, and f) MnSb<sub>2</sub>O<sub>x</sub>.

## References

1. R. K. Karlsson and A. Cornell, *Chem. Rev.*, 2016, **116**, 2982-3028.
2. H. A. Hansen, I. C. Man, F. Studt, F. Abild-Pedersen, T. Bligaard and J. Rossmeisl, *Phys. Chem. Chem. Phys.*, 2010, **12**, 283-290.
3. K. S. Exner, J. Anton, T. Jacob and H. Over, *Angew. Chem. Int. Ed.*, 2014, **53**, 11032-11035.
4. C. A. Martinez-Huitle and S. Ferro, *Chem. Soc. Rev.*, 2006, **35**, 1324-1340.
5. L. Nanni, S. Polizzi, A. Benedetti and A. D. Battisti, *J. Electrochem. Soc.*, 1999, **146**, 220-225.
6. R. K. B. Karlsson, H. A. Hansen, T. Bligaard, A. Cornell and L. G. M. Pettersson, *Electrochim. Acta*, 2014, **146**, 733-740.
7. K. Xiong, Z. Deng, L. Li, S. Chen, M. Xia, L. Zhang, X. Qi, W. Ding, S. Tan and Z. Wei, *J. Appl. Electrochem.*, 2013, **43**, 847-854.
8. N. Menzel, E. Ortel, K. Mette, R. Kraehnert and P. Strasser, *ACS Catal.*, 2013, **3**, 1324-1333.
9. H. Cao, D. Lu, J. Lin, Q. Ye, J. Wu and G. Zheng, *Electrochim. Acta*, 2013, **91**, 234-239.
10. S. Trasatti, *Electrochim. Acta*, 1984, **29**, 1503-1512.
11. A. R. Zeradjanin, N. Menzel, W. Schuhmann and P. Strasser, *Phys. Chem. Chem. Phys.*, 2014, **16**, 13741-13747.
12. T. Loucka, *J. Appl. Electrochem.*, 1990, **20**, 522-523.
13. H. B. Beer, *U.S. Patent 4052271*, 1977.
14. I. A. Moreno-Hernandez, C. A. MacFarland, C. G. Read, K. M. Papadantonakis, B. S. Brunshwig and N. S. Lewis, *Energy Environ. Sci.*, 2017, **10**, 2103-2108.
15. A. Jain, S. P. Ong, G. Hautier, W. Chen, W. D. Richards, S. Dacek, S. Cholia, D. Gunter, D. Skinner, G. Ceder and K. A. Persson, *APL Mater.*, 2013, **1**, 011002.
16. H. Bisht, H.-T. Eun, A. Mehrstens and M. A. Aegerter, *Thin Solid Films*, 1999, **351**, 109-114.
17. G. Westin and M. Nygren, *J. Mater. Chem.*, 1993, **3**, 367-371.
18. M. C. Biesinger, L. W. Lau, A. R. Gerson and R. S. Smart, *Phys. Chem. Chem. Phys.*, 2012, **14**, 2434-2442.
19. R. Izquierdo, E. Sacher and A. Yelon, *Appl. Surf. Sci.*, 1989, **40**, 175-177.
20. M. C. Biesinger, B. P. Payne, A. P. Grosvenor, L. W. M. Lau, A. R. Gerson and R. S. C. Smart, *Appl. Surf. Sci.*, 2011, **257**, 2717-2730.
21. A. Aoki, *Jpn. J. Appl. Phys.*, 1976, **15**, 305-311.
22. G. I. Straguzzi, K. B. Bischoff, T. A. Koch and G. C. A. Schuit, *J. Catal.*, 1987, **103**, 357-365.
23. M. C. Biesinger, B. P. Payne, L. W. M. Lau, A. Gerson and R. S. C. Smart, *Surf. Interface Anal.*, 2009, **41**, 324-332.

24. X. Zhu, P. Wang, Z. Wang, Y. Liu, Z. Zheng, Q. Zhang, X. Zhang, Y. Dai, M. Whangbo and B. Huang, *J. Mater. Chem. A*, 2018, **6**, 12718-12723.
25. M. Jiang, H. Wang, Y. Li, H. Zhang, G. Zhang, Z. Lu, X. Sun and L. Jiang, *Small*, 2017, **13**.
26. K. Cho and M. R. Hoffmann, *Chem. Mater.*, 2015, **27**, 2224-2233.
27. P. C. K. Vesborg and T. F. Jaramillo, *RSC Adv.*, 2012, **2**, 7933.
28. E. M. Aghae, M. Alimohammadi, R. Nabizadeh, G. J. Khaniki, S. Naseri, A. H. Mahvi, K. Yaghmaeian, H. Aslani, S. Nazmara, B. Mahmoudi and M. Ghani, *J. Environ. Health Sci. Eng.*, 2014, **12**, 133.